Acta Materialia 201 (2020) 504–516

Contents lists available at ScienceDirect

Acta Materialia

journal homepage: www.elsevier.com/locate/actamat

Irradiation induced void spheroidization, shrinkage and migration in Cu at elevated temperatures: An *in situ* study

Cuncai Fan[a,*], Rayaprolu Goutham Sreekar Annadanam[a], Zhongxia Shang[a], Jin Li[a], Meimei Li[b], Haiyan Wang[a,c], Anter El-Azab[a,d], Xinghang Zhang[a,*]

[a] School of Materials Engineering, Purdue University, West Lafayette, IN 47907, United States
[b] Nuclear Engineering Division, Argonne National Laboratory, Argonne, IL 60439, United States
[c] School of Electrical and Computer Engineering, West Lafayette, IN 47907, United States
[d] School of Nuclear Engineering, Purdue University, West Lafayette, IN 47907, United States

ARTICLE INFO

Article history:
Received 4 July 2020
Revised 29 September 2020
Accepted 4 October 2020
Available online 7 October 2020

Keywords:
In situ irradiation
Spheroidization
Void migration
Stacking fault tetrahedron
Phase-field modeling

ABSTRACT

Understanding the void evolution in irradiation environment is of great interest and significance, as irradiation-induced voids typically lead to pronounced volumetric swelling and degradation of mechanical properties. *In situ* studies on the irradiation response of nanovoids at elevated temperature remain limited. In this work, we performed systematic *in situ* 1 MeV Kr^{++} irradiations on Cu with nanovoids in a transmission electron microscope up to 350 °C. The *in situ* studies revealed intriguing void spheroidization, shrinkage and migration. Furthermore, the morphology evolution and migration of nanovoids showed a strong dependence on irradiation temperature and initial void size. Post-irradiation analyses identified defect clusters in the form of stacking fault tetrahedrons, and the remaining large faceted nanovoids. The underlying mechanisms of irradiation-induced void spheroidization and shrinkage were discussed based on phase-field modeling.

Published by Elsevier Ltd on behalf of Acta Materialia Inc.

1. Introduction

In the past decades, the formation and growth of irradiation-induced voids (or bubbles) have been extensively investigated because of their profound impact on the microstructure and mechanical properties of irradiated materials [1–5]. As a typical type of vacancy clusters in solids, voids are widely observed in metals and alloys after their irradiations by energetic particles, such as electrons [6], protons [7], neutrons [8] and ions [9,10]. The phenomenon of volumetric expansion accompanied with voids in irradiated materials is commonly referred to as void swelling [11–13]. Void swelling often leads to degradation of the mechanical properties via irradiation hardening, embrittlement, and premature fracture [14–16]. To design advanced materials for future nuclear reactors, it is essential to explore how voids evolve under the irradiation environment [17].

Considering efficiency and safety, ion irradiation has been widely used for emulating the void evolutions in nuclear reactors in spite of the existence of numerous microstructure and properties differences induced by the two techniques [18]. Prior investigations showed that void swelling involves thermodynamic factors, such as surface energy increase or decrease, as well as kinetic factors governed by interfacial reactions and reactions of defects with sinks [19–22]. According to early experimental studies, several major characteristics of void swelling have been resolved. First, void nucleation and growth show a strong dependence on irradiation temperature and the magnitude of void swelling often peaks at intermediate temperatures in the range of 0.25 to 0.60 T_m (melting temperature) [3,23,24] . In principle, at low temperatures, void growth is limited by insufficient vacancy diffusivity, while at very high temperatures it is suppressed by a loss of vacancy supersaturation, because of the accelerated recombination between opposite type of defects and the approach of the defect concentration to the thermal equilibrium value [25]. Second, in most cases, the geometry of irradiation-induced voids cannot be simply described as perfect spheres [21]. A couple of complex configurations have been reported, involving shape variations among different materials [19,26–28]. Due to surface energy anisotropy, the voids in crystalline metals often exhibit distinct facets corresponding to low-index close-packed planes [26]. For instance, different faceted voids were found in irradiated Ni [21], Al [29], Mg [30], Cu [3], Fe [31], Cu-Ni alloys [28], and steels [32]. Moreover, there are other factors that may influence the irradiation-induced void swelling, such as the inert gas [33], solute atoms [34], biased sinks [35], dose

* Corresponding authors
E-mail addresses: cuncaifan@gmail.com (C. Fan), xzhang98@purdue.edu (X. Zhang).

https://doi.org/10.1016/j.actamat.2020.10.008
1359-6454/Published by Elsevier Ltd on behalf of Acta Materialia Inc.

and dose rate [36], as well as external stress [37]. The theoretical underpinning for void evolution at elevated temperatures, propounded based on experimental observations, can only be verified by testing the postulates through simulations. Therefore, we performed phase-field simulations for validating the proposed mechanisms.

Theoretically, void nucleation and growth have been studied using the classical nucleation theory [38], chemical rate theory approach [23,39,40] and cluster dynamics [41,42]. Recently, the phase-field approach has proved to be an effective method for capturing the morphological evolution of interfaces in various materials science processes at diffusive time scales [43], and it has been successfully applied to describing the void formation and evolution in irradiated metals [22,44–48]. We used a phase field approach to explain the shrinkage of the nanovoids (NVs) in single-crystalline Cu (110) observed during *in situ* 1 MeV Kr^{++} radiation at room temperature (RT) [49]. However, a systematic experimental study coupled with phase field simulation that considers the influence of temperature on the irradiation response of NVs is still lacking. In this work, we investigated the temperature dependent heavy ion irradiation damage in Cu (110) films with NVs. *In situ* heavy ion irradiations were performed in a transmission electron microscope (TEM) at elevated temperatures between 190 and 350 °C. The irradiation temperatures cover the onset and peak welling regimes for Cu [50]. Our experimental study combined with phase-field simulations provides new insights for understanding the radiation response of voids in solids.

2. Experimental

Cu films, ~ 2 μm thick, were deposited on HF-etched Si (112) substrates at RT by using magnetron sputtering with an ultrahigh purity (99.995 wt.%) Cu target. Before deposition, the chamber was evacuated to a base pressure $< 8 \times 10^{-8}$ torr. The deposition rate was controlled at ~ 0.6 nm/s. After deposition, the film texture was analyzed using an X-ray diffractometer with a Cu Kα1 source.

Plan-view and cross-section TEM specimens were prepared by polishing, dimpling, and low energy (3.5 keV) Ar ion milling. Before and after irradiations, the specimens were carefully examined by a Thermo-Fischer Scientific/FEI Talos 200X analytical microscope operated at 200 kV. The *in situ* heavy-ion irradiations were conducted in the Intermediate Voltage Electron Microscope (IVEM) at Argonne National Laboratory, where an ion accelerator is attached to a Hitachi-900 TEM. Three different TEM specimens were pre-annealed at the irradiation temperatures for ~ 0.5 h, and then irradiated by 1 MeV Kr^{++}, respectively, at 190, 250 and 350 °C. Before irradiations, the temperature calibration for TEM holder and specimens was conducted in a vacuum chamber with a thermocouple spot weld on a disk specimen. The temperature variance between the controller and the sample was found to be within $\pm$ 3 °C.

The radiation dose (in dpa) was calculated using Stopping and Range of Ions in Matter (SRIM) 2008 with Kinch-Pease method [51,52], with a displacement threshold energy of 30 eV for Cu [25]. The calculations indicate that > 99% Kr ions transmitted through the TEM foils, and more detailed SRIM calculation results can be found elsewhere [53]. The maximum dose was ~ 0.5 dpa for the irradiation at 190 °C, and 1.0 dpa for the cases at 250 and 350 °C, with the same dose rate around 3×10^{-4} dpa/s.

3. Results

3.1. Faceted nanovoids in as-deposited cu (110) films

Fig. 1(a) shows the conventional $\theta-2\theta$ XRD profile of Cu film and Si substrate, and Fig. 1(b) shows the (110) and (100) φ-scan profiles of Si substrate (blue) and Cu film (red), respectively. These XRD results indicate an epitaxial growth of Cu (110) film on the Si (112) substrate, and the corresponding film-substrate orientation relationship is summarized and schematically illustrated in Fig. 1(c): Cu (110) // Si (112), Cu [$1\bar{1}0$] // Si [$\bar{1}\bar{1}1$] and Cu [001] // Si [$\bar{1}10$]. The plan-view TEM micrographs recorded at under-focus ($\Delta f = -1.5$ μm) and over-focus ($\Delta f = +1.5$ μm) imaging conditions along beam direction $\boldsymbol{B}$ = [110] in Fig. 1(d) and (e) show the formation of faceted NVs with dark or white Fresnel fringes. In addition, the inserted selected area diffraction (SAD) pattern in Fig. 1(e) confirms single-crystal-like diffraction spots of Cu (110). The enlarged view of a high-resolution TEM (HRTEM) image in Fig. 1(f) reveals the NV is primarily faceted on the {111} plane and elongated along the ⟨112⟩ direction. The cross-section TEM micrographs in Fig. 1(g) and (h) taken at an under-focus ($\Delta f = -1.5$ μm) condition display the cylindrical nanovoids along the film growth direction. The inserted SAD patterns in Fig. 1(g) and (h) show clear evidence of single-crystal-like diffraction respectively along the beam directions of $\boldsymbol{B}$ = [$1\bar{1}0$] and [001]. The HRTEM micrograph in Fig. 1(i) (recorded along $\boldsymbol{B}$ = [001]) characterizes an elongated NV along the growth direction. In order to describe the configuration of such faceted NVs, three dimensional parameters are defined as follows: the void length *L*, width *W*, and height *H*. As marked in Fig. 1(f) and (i), *L* and *W* describe the projected dimensions in plane-view image, while *H* refers to the dimension along the growth direction in the cross section. Statistic studies show that the mean value is 17 nm for *L*, 7 nm for *W*, and 20 nm for *H*. The TEM foil thickness was measured as ~ 115 nm using the convergent beam electron diffraction (CBED) technique (see Supplementary Figure S1) [54]. Since the TEM foil thickness is much higher than void dimensions, the as-deposited NVs are assumed to be embedded inside the TEM specimens.

3.2. Irradiation-induced void spheroidization and shrinkage

In situ TEM radiation makes it possible to directly observe the void morphology evolution during an irradiation process. It should be emphasized that the experimental results presented in the following sections are based on the observations of an area of 450 × 450 nm^2, and a moderate set of nanovoids limited by the manpower available for data analyses. The evolutions of microstructures up to 0.2 dpa at three different irradiation temperatures are compiled in Fig. 2. With increasing dose, it is evident that the preexisting faceted NVs undergo spheroidization through the reduction of void length *L* and the simultaneous expansion of void width *W*. The spheroidization rate tends to increase with increasing temperature. Consequently, by 0.20 dpa, most NVs irradiated at higher temperatures, 250 and 350 °C, have fully spheroidized as shown in Fig. 2(b5) and (c5). More detailed observations on the irradiation-induced void spheroidization can be found in Supplementary Video SV1-SV3.

At a high dose > 0.30 dpa, the irradiated NVs showed little change in shape, but they shrank gradually. Fig. 3 compares the TEM micrographs for void shrinkage at different irradiation temperatures from 0.3 to 1.0 dpa. With increasing dose, it is evident that the spheroidized NVs shrank continuously until they became too tiny to be resolved by TEM. Three representative NVs showing the typical void shrinkage behaviors are marked by circles. Note that the shrinkage process also shows a strong dependence on temperature. As shown in Fig. 3, at a given dose level the mean NV size increases with increasing irradiation temperature, indicting the shrinkage rate decreases with increasing temperature.

In Fig. 3(c1)-(c5), all the NVs irradiated at 350 °C remain their circular shape while shrinking continuously at a higher dose. However, at 250 °C some of the fully spheroidized NVs occasionally presented 'craters' on their surfaces. Two of such peculiar 'imper-

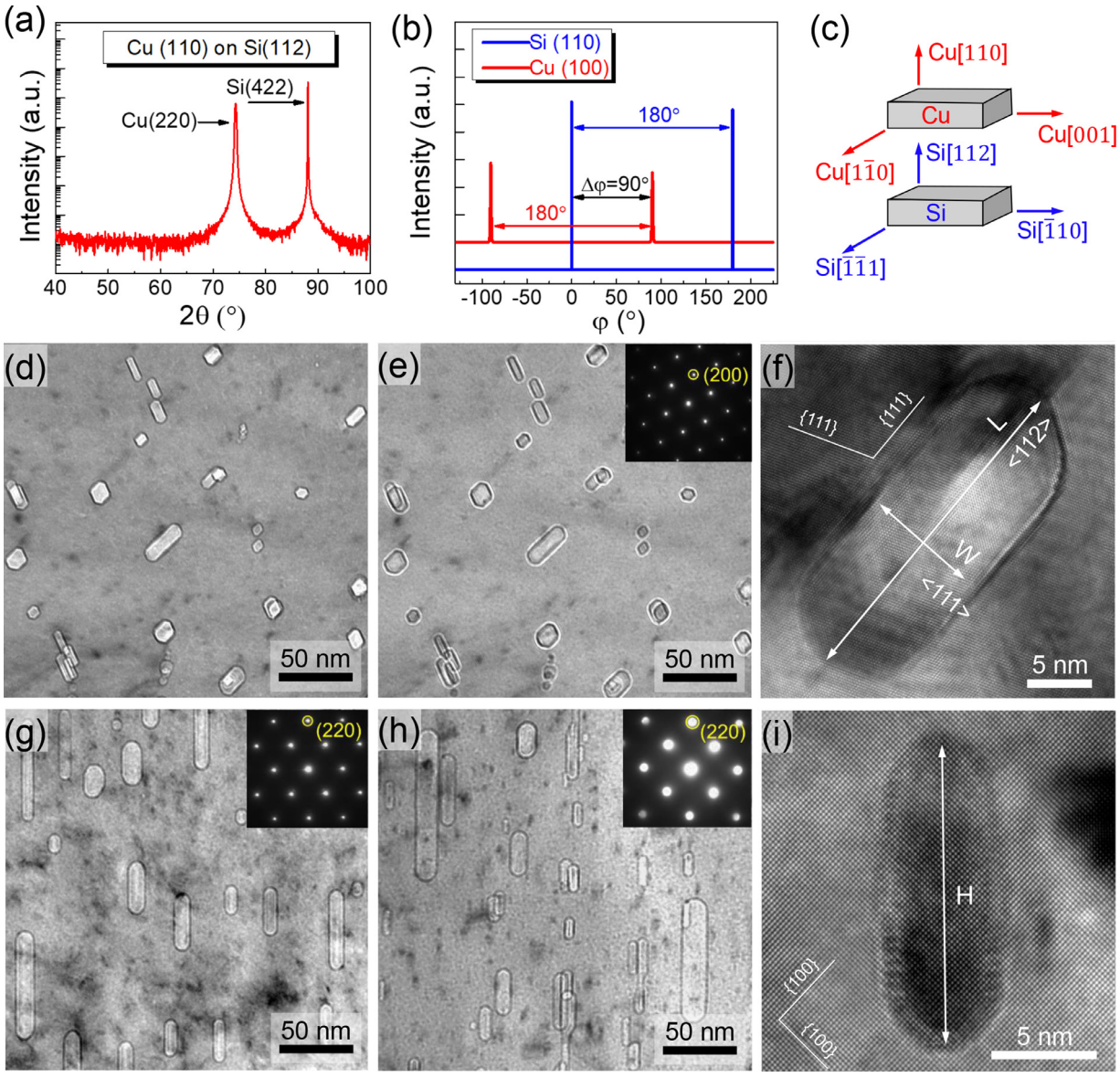

Fig. 1. Texture analysis, and microstructure characterization of as-deposited NV-Cu (110) films. (a) $\theta-2\theta$ XRD profile of sputtered film showing the epitaxial growth of Cu (110) on Si (112) substrate. (b) XRD φ-scan of Cu {100} (red) and Si {110} (blue). (c) Schematic illustration of film-substrate orientation relationship. (d)-(f) Plan-view TEM micrographs of faceted nanovoids in as-deposited Cu films. *L* and *W* in (f) mark the length and width of an elongated nanovoid. (g)-(i) Cross-sectional TEM micrographs of faceted nanovoids along growth direction. The *H* in (i) denotes the height of a cylindrical nanovoid. (For interpretation of the references to colour in this figure legend, the reader is referred to the web version of this article.)

fect' NVs are marked by the arrows in the insets of Fig. 3(b3) and (b4). It was found that the imperfect voids were able to recover from eclipse features (self heal). One typical example is summarized and shown in Fig. 4. As shown in Fig. 4(a1), a circular large void was measured to be 15 nm in diameter at 0.559 dpa. The void became concaved from its lower left corner as marked by the arrow in Fig. 4(a2), and the concavity eroded into the void during irradiation shown in Fig. 4(a3)-(a4). After a while, the void recovered its spherical geometry at 0.656 dpa as shown in Fig. 4(a5). During subsequent irradiation, a similar concave process repeated from lower right portion of the void, followed by its recovery as shown in Fig. 4(b1)-(b5). By 0.766 dpa in Fig. 4(b5), the void had decreased its diameter from 15 to 12 nm. In addition, some irradiation-induced defect clusters were captured in the vicinity of the NV, as shown in Fig. 4(a5) and (b1). These defect clusters are assumed to be SFTs based on our subsequent post-irradiation analyses. The *in situ* TEM observation of Fig. 4 can be found in Supplementary Video SV4.

To quantify the morphology evolution of NVs, two parameters are defined as follows. First, the aspect ratio $\mu = W/L$ was used to describe the spheroidization process. Second, the porosity *P* was defined to describe the shrinkage process by taking into the consideration of both void size *D* (diameter) and density, given by:

$$P = \frac{\sum V_i}{St} \tag{1}$$

where ΣV_i is the sum of the volume for observed NVs, *S* is the observed area ~ 0.18 μm^2, and *t* is the TEM foil thickness, approximately 115 nm. For each case, more than 20 NVs were manually measured based on the *in-situ* videos SV1-SV3. Fig. 5 summarizes the variations of μ and *P* with increasing dose Φ at different irradiation temperatures. It shows that the void spheroidization occurred primarily at low dose (< 0.3 dpa) through the reduction of void length *L* and extension of void width *W*, leading to the increase of μ demonstrated in Fig. 5(a). Before irradiation, μ had an initial value of 0.4 because of the elongation of the NVs along

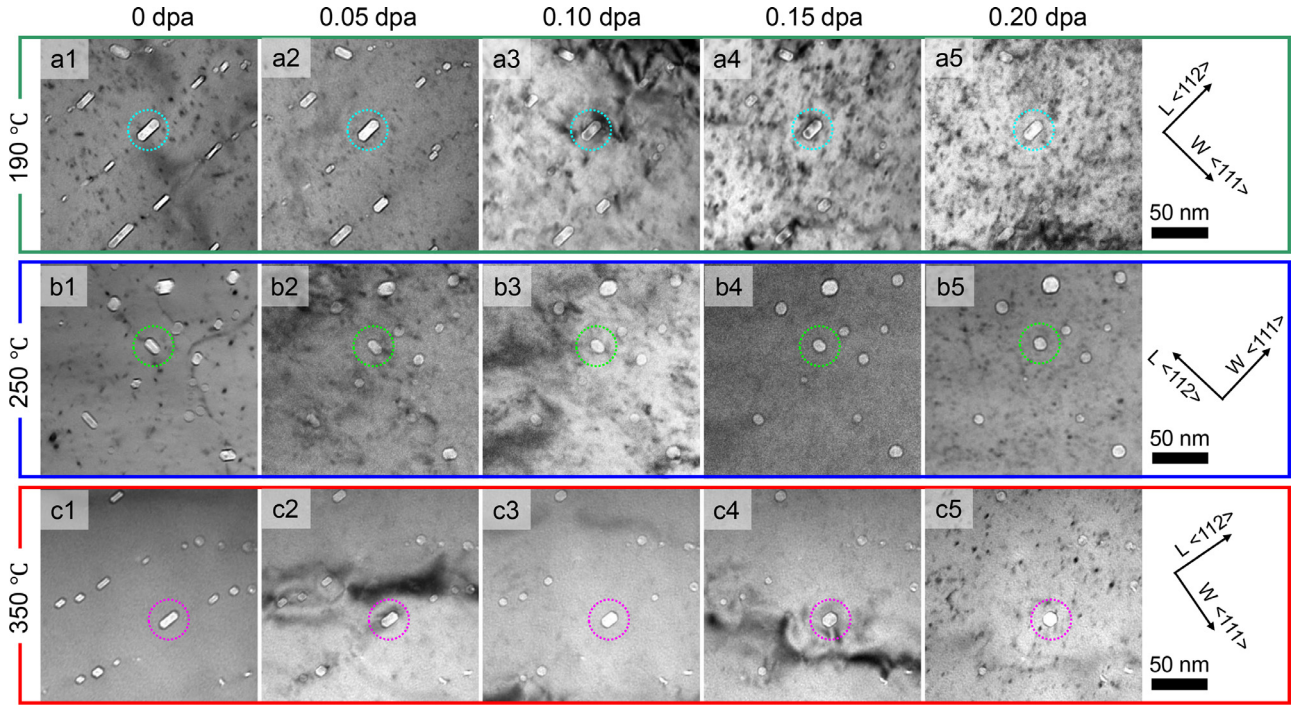

Fig. 2. TEM sequential snapshots demonstrating the spheroidization process of faceted nanovoids at low dose < 0.2 dpa and various temperatures: (a1)-(a5) 190 °C, (b1)-(b5) 250 °C, and (c1)-(c5) 350 °C. The corresponding *in situ* videos can be found in Supplementary Videos SV1-SV3.

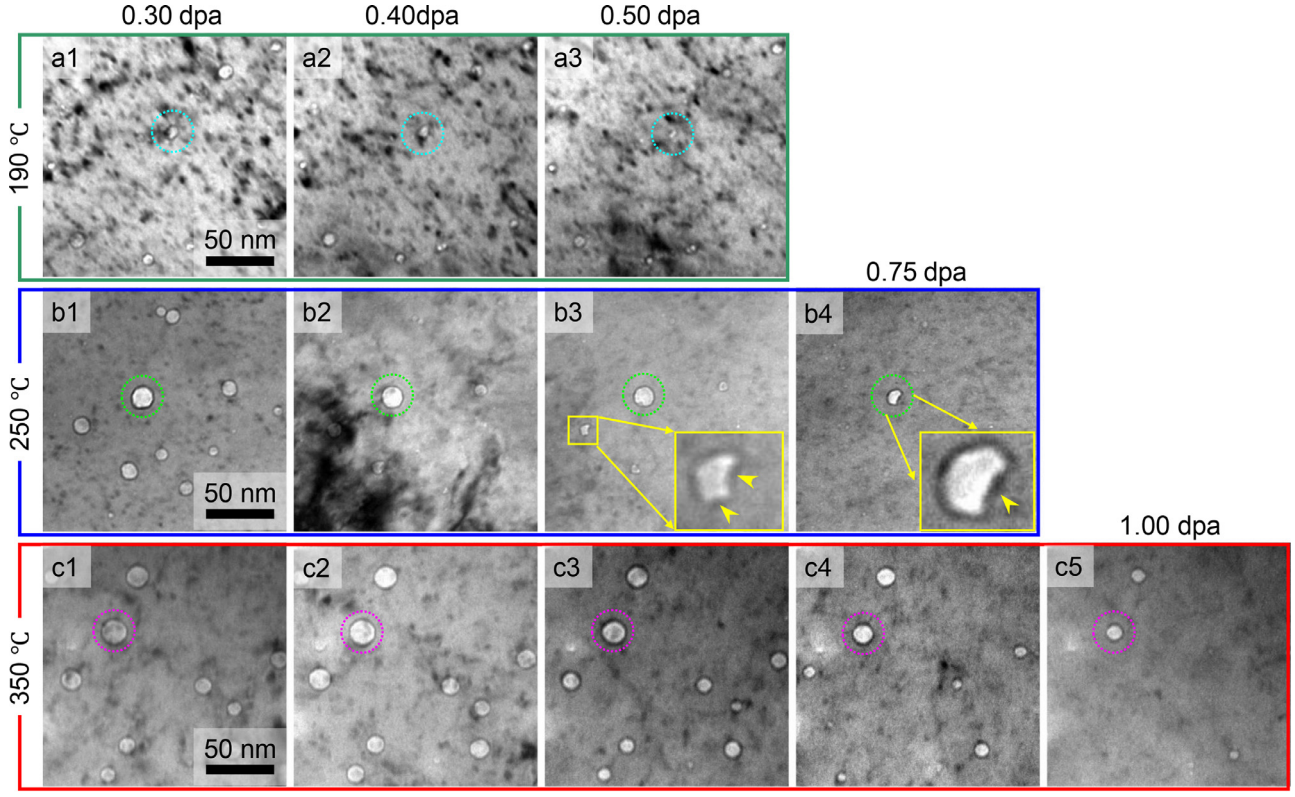

Fig. 3. TEM snapshots demonstrating the shrinkage process of spherical nanovoids at higher doses over 0.3–1.0 dpa and various temperatures: (a1)-(a3) 190 °C, (b1)-(b4) 250 °C, and (c1)-(c5) 350 °C. The insets in (b3) and (b4) denote two peculiar NVs that contracted locally at 250 °C.

<112> direction, as shown in Fig. 1(f). With increasing radiation dose, μ increased gradually, and by 0.2 dpa it nearly reached the unity at 350 °C, 0.96 at 250 °C, and 0.84 at 190 °C. In addition to the current studies at high temperatures, a reference of the variation of μ at RT is also plotted in black squares in Fig. 5(a) [49]. It is worth pointing out that although μ also increases slightly at RT, such increment arises from the different reduction rates in both *L* and *W*, possibly caused by the effect of void surface curvature on the interstitial diffusion [49]. At a higher dose (> 0.3 dpa), the aspect ratio μ barely changed, so the voids could be regarded

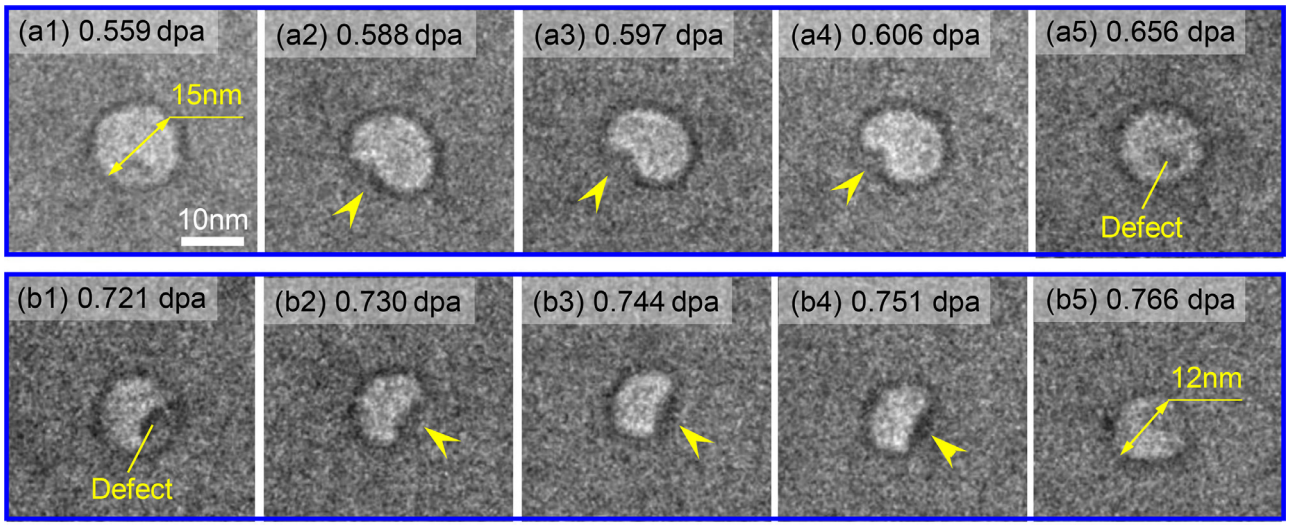

Fig. 4. Morphology evolution of a void irradiated at 250 °C. The arrows mark irradiation-induced 'craters' on the void surface. The corresponding *in situ* TEM video can be found in SV4.

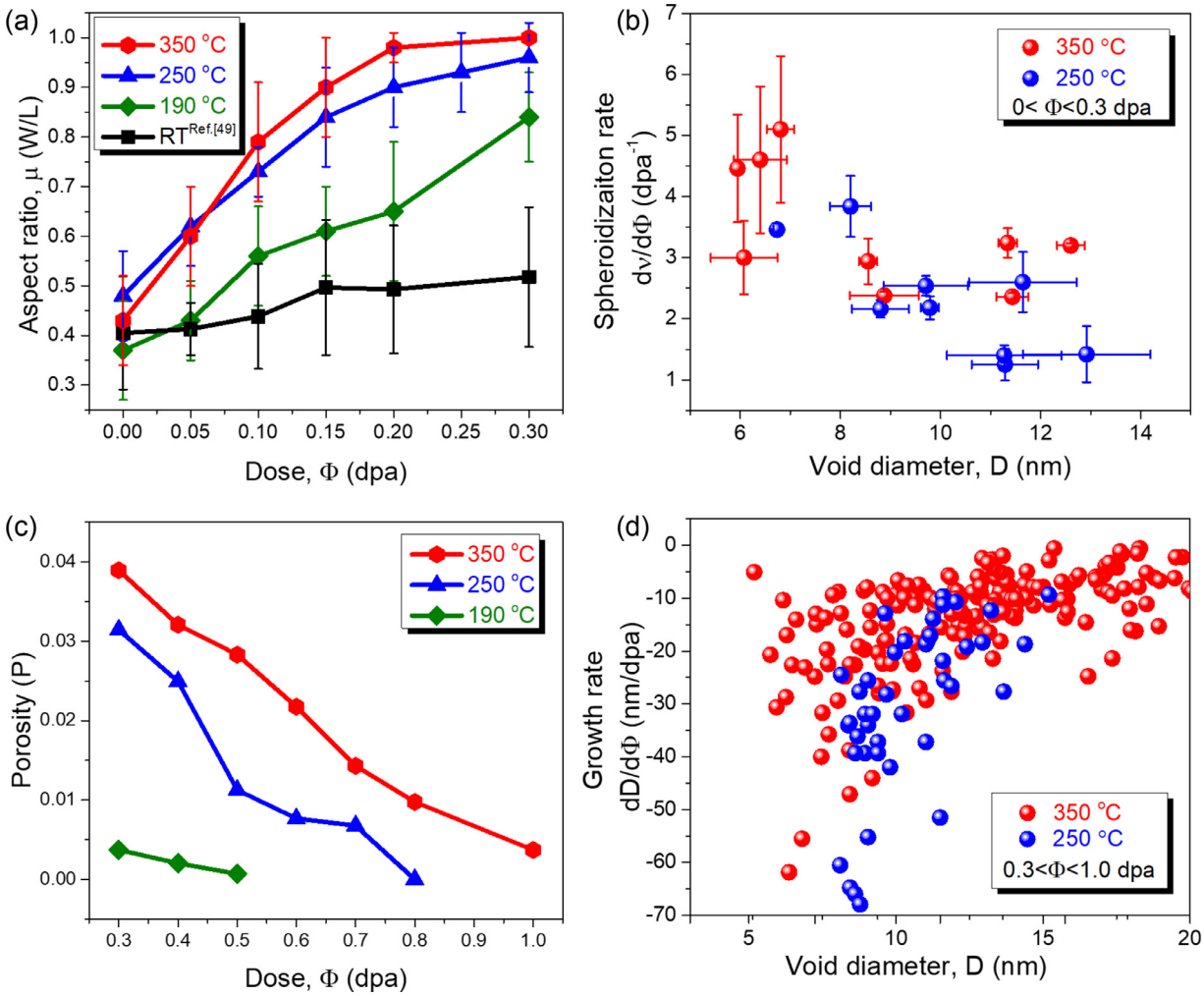

Fig. 5. The influences of irradiation temperature and void size on void spheroidization and shrinkage. (a) Variation of aspect ratio μ (W/L) with increasing dose Φ to 0.3 dpa. A reference data set [49] of RT irradiation is also plotted in black squares. (b) The spheroidization rate ($d\mu/d\Phi$) *versus* void diameter D. (c) Variation of porosity P with increasing dose Φ over 0.3–1.0 dpa. (d) The void growth rate ($dD/d\Phi$) *versus* void diameter D.

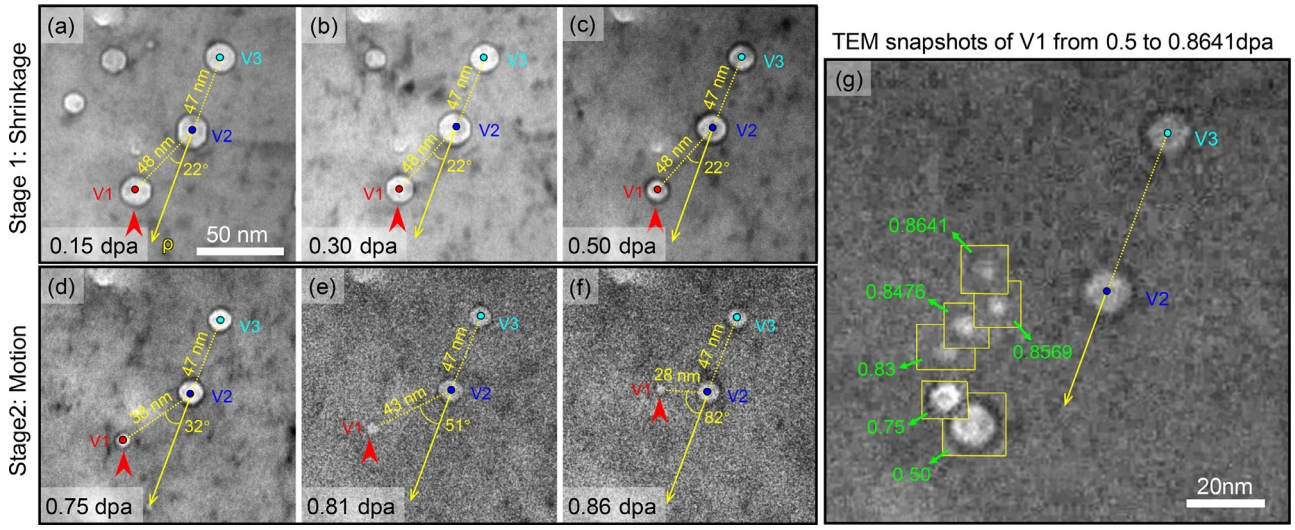

Fig. 6. Irradiation-induced void shrinkage and migration at 350 °C. (a)-(c) Shrinkage of void V1 from 0.15 to 0.50 dpa. (d)-(f) Migration of void V1 during irradiation from 0.75 to 0.86 dpa. (g) The compiled TEM snapshots at different doses (marked by numbers) clearly demonstrate the shrinkage and migration of small void V1 with increasing dose. More detailed information can be found in Supplementary Video SV6.

as spheres; its volume or size, therefore, would be easily calculated using its diameter *D*. Fig. 5(b) shows that the spheroidization rate ($d\mu/d\Phi$) is greater for the smaller faceted NVs. The calculated porosity decreases with increasing dose (0.3–1.0 dpa) as shown in Fig. 5(c). Furthermore, at a given dose level the porosity declines with decreasing temperature, suggesting the void shrinkage process is suppressed at higher temperature. Moreover, the variation of growth rate ($dD/d\Phi$) in Fig. 5(d) reveals that smaller spherical NVs appear to shrink faster for specimens irradiated at 250 and 350 °C.

3.3. Irradiation-induced void migration at 350 °C

In addition to void spheroidization and shrinkage, we also captured the irradiation-induced void migration at 350 °C. The accelerated (by 32 times) *in situ* TEM video in Supporting Video SV5 shows that during 1 MeV Kr ion irradiation, from 0.25 to 1.00 dpa at 350 °C, some small voids were obviously changing their positions. We carefully examined 35 NVs in total, as labeled in Supplementary Figure S1, and 25 of them started migrating only when the void diameter reduced to several nanometers. One typical example of irradiation-induced void shrinkage and migration is shown in Fig. 6. As shown in Fig. 6(a)-(c), there are three voids labelled as V1-V3, and they all remained stationary while shrinking gradually from 0.15 to 0.50 dpa. The position of void V1 relative to V2 and V3 was measured and marked in Fig. 6(a). With increasing dose, V1 was changing its position and started migrating over 0.50 dpa until it eventually disappeared by ~0.86 dpa, as demonstrated in Fig. 6(d)-(f). Such irradiation-induced void shrinkage and migration can be better visualized in Fig. 6(g) where the successive TEM snapshots of void V1 from 0.50 to 0.8641 dpa are complied. The corresponding video for Fig. 6 can be found in Supplementary Video SV6.

As the large voids remained mostly stationary, like the V2 and V3 in Fig. 6, they were taken as reference points for measuring the relative positions of mobile voids at different doses. Consequently, the void cumulative migration distance λ, instantaneous migration velocity *v*, and migration trajectories can be calculated. As shown in Fig. 7a, 25 out of 35 voids migrated by a long distance >20 nm before they vanished. The maximum migration distance λ_{max} is ~ 127 nm, and the average migration distance λ_{ave} is 50 nm, around half of the TEM foil thickness. The logarithmic plot of void migration velocity *v* in Fig. 7(b) reveals that ln *v* is inversely proportional to void diameter *D* and can be empirically described by:

$$\ln v = C_0 + \frac{C}{D} \tag{2}$$

where C_0 and *C* are coefficients that may depend on the irradiated materials and radiation conditions. Evident migrations, defined as $v > 0.1$ nm/s, mostly occurred for smaller NVs with a dimeter $D < 6.5 \pm 1.5$ nm. Moreover, the migration trajectories in Fig. 7(c) indicate that small NVs tend to migrate in all directions. Some of them might be confined at a local region and migrate back and forth from time to time, while others might migrate continuously along one direction. It seems that the void migration is analogous to Brownian motion and follows a random walk under irradiation environment at high temperature.

3.4. Post-irradiation analysis

To identify the radiation-induced defect clusters, post-irradiation TEM analysis was performed. The TEM results in Fig. 8(a)-(c) reveal that high-density stacking fault tetrahedrons (SFTs) were produced in all specimens regardless of temperature. Fig. 8(d) compares the SFT edge length (L_{SFT}) distributions, and it shows that the average value of L_{SFT} increases slightly with increasing temperature, ranging from 1 to 7 nm, in good agreement with previous reports on the radiation-induced SFTs in Cu [49,55,56]. Conversely, the SFT density ρ_{SFT} decreases monotonically at higher temperature, as shown in Fig. 8(e). The correlation between the SFT edge length (L_{SFT}) and the number of vacancies (N_V) is given by [57]:

$$N_V = 3\left(\frac{L_{SFT}}{a}\right)^2 \tag{3}$$

where *a* is the lattice parameter, 0.3615 nm for Cu. Using Eq. (3), the vacancy concentration (C_v) stored in SFTs can be expressed as:

$$C_v = N_v \frac{\rho_{SFT} M}{\rho N_A} \tag{4}$$

where N_A is the Avogadro's number, ρ is matrix density (8.92 g/cm^3 for Cu), and *M* is material atomic mass (63.55 g/mol

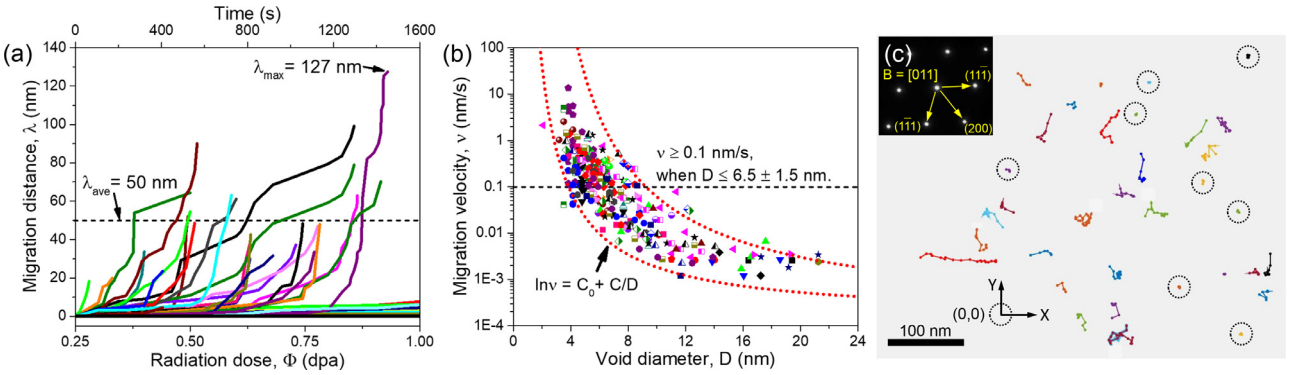

Fig. 7. Statistic studies on the radiation-induced void migration. (a) The void migration distance λ is plotted as a function of irradiation dose Φ. (b) The logarithmic plot of void migration velocity *v* against void diameter *D*. (c) Trajectories of all the inspected voids, indicating their random walks through the crystalline lattice. The SAD insert shows single crystal-like diffraction along the Cu <011> zone axis.

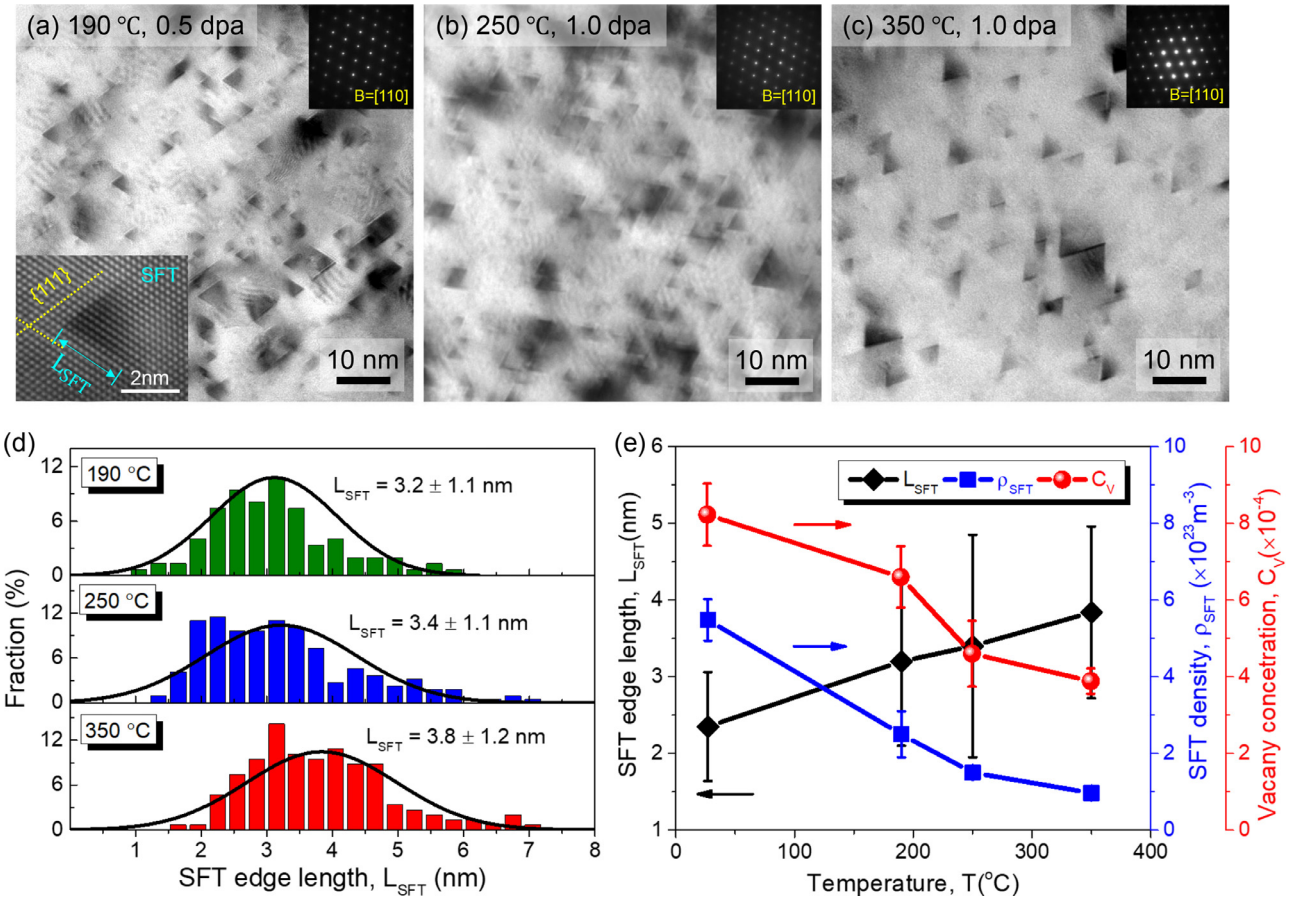

Fig. 8. Irradiation-induced SFTs. (a)-(c) Post-irradiation TEM micrographs examined along Cu <110> zone axis (evidenced by SAD patterns) showing triangular-shape SFTs at all temperatures. The lower left inset in (a) is the HRTEM image of a representative SFT with its edge length marked by L_{SFT}. (d) Size distributions of SFTs at various irradiation temperatures. (e) Variations of SFT size (L_{SFT}), density (ρ_{SFT}) and its corresponding vacancy concentration (C_v). The data points of RT irradiation from [49] are also plotted in (e).

for Cu). The calculated C_v is also plotted in Fig. 8(e), and it decreases with increasing temperature.

In addition to SFTs, the TEM images in Fig. 9 compare the configurations of two representative NVs after the irradiation at 350 °C to 1 dpa. Fig. 9(a) shows a small circular-shape NV, around 10 nm in diameter, surrounded by numerous SFTs. Nevertheless, the large NV in Fig. 9(b), around 23 nm in diameter, still have several facets that are indexed as {111}, {200}, {113} and {510} crystal planes based on the inset SAD pattern.

3.5. Phase-field modeling

To understand the underlying mechanism of the void evolution caused by high-temperature irradiation, we performed phase field simulations in two-dimensions with a thin film configuration. Phase-field models are mesoscale microstructure simulating tools, which come under the category of field-theoretic models, used to capture the nucleation and growth kinetics of voids simultaneously. The phase-field employed here, found elsewhere in [42,45], contains both vacancies and interstitials with biased source terms.

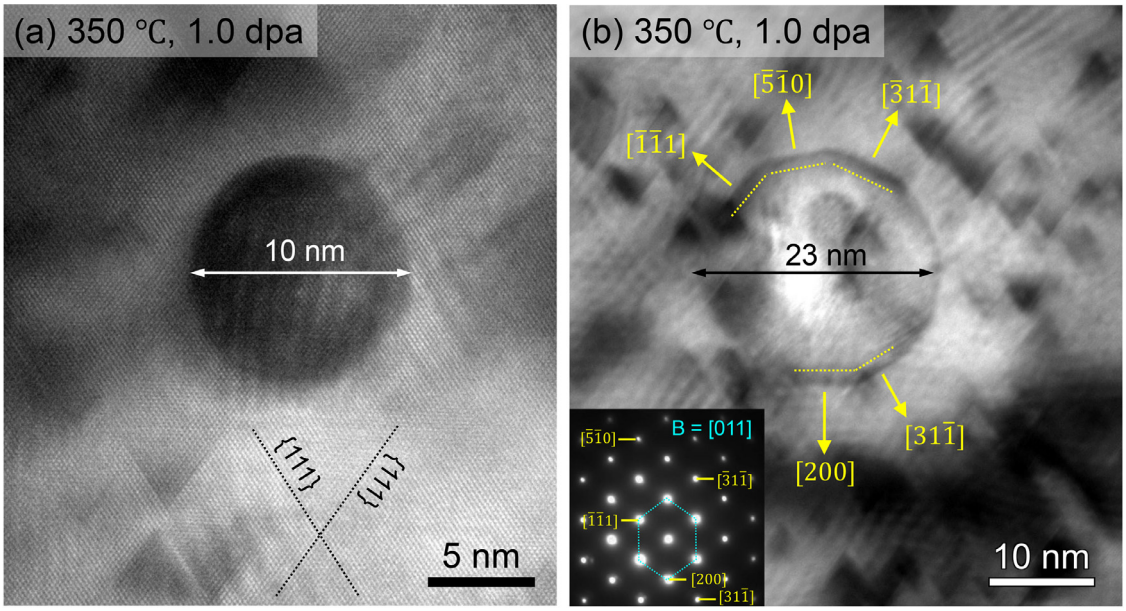

Fig. 9. Post-irradiation analysis of remaining nanovoids after 1.00 dpa irradiation at 350 °C. (a) A small NV with a diameter of 10 nm. (b) A large NV with a diameter of 23 nm has facets on several low-index crystallographic planes.

The simulation domain has a total of 231 × 151 grid points, with the solid region occupying 151 × 151 grid points and the rest being empty space on both sides of the film. A void that is 30 × 13 grid point with an aspect ratio of 0.43 was initialized at the center of the film. The initial condition can be found in Supplementary Figure S2, and the currently used model was developed and reported elsewhere [58]. In our simulations, the concentration of the point defects in the solid region is taken to be thermally equilibrium. The equations are non-dimensionalized to qualitatively describe the temperature effect on void evolution through the control parameter D_v/D_i. The ratios of the normalized point-defect diffusivities, D_v/D_i, are set as 0.02, 0.33, and 0.67 to qualitatively model void evolution at low, medium, and high temperature, respectively. Although radiation produces equal number of vacancies and interstitials, in Cu some of the vacancies agglomerate in the form of SFTs (see Fig. 8) that are immobile and cannot interact with pre-existing NVs. To account for such effect, we have, in our model, assumed a biased cascade source. For low-temperature irradiation, the number of vacancies introduced in each cascade event is only 90% of the number of interstitials; for the medium and high temperature cases, the number of vacancies introduced in each cascade event is 95% of the number of interstitials. In addition, the surface energy anisotropy is also included in the current model by making the gradient coefficients of the phase field variable orientation dependent, as what has been reported in another independent study [47].

The simulation results are summarized in Fig. 10. The snapshots of vacancy concentration C_v in Fig. 10(a1)-(c7) compare the radiation-induced void spheroidization and shrinkage at different temperatures. The corresponding dimensional changes of void length L and width W are plotted as a function of time τ in Fig. 10(d1)-(d3). Note that in Fig. 10(d1), both L and W decreased with increasing time at low radiation temperature, but the reduction rate of L is greater than that of W. In Fig. 10(d2) and (d3), however, W initially increased until it reached L, but then both of them decreased thereafter. As a result, the void underwent a spheroidization process with its aspect ratio of W/L increasing rapidly from 0.43 to 1.00, as shown in Fig. 10(e1). Meanwhile, the void kept shrinking for all the cases, as indicated by the void area A reduction in Fig. 10(e2). Especially, Fig. 10(e1) and (e2) also suggest that, with increasing temperature, the radiation-induced spheroidization is promoted, while the shrinkage process is suppressed. In conclusion, these simulation results qualitatively agree with our experimental findings in Figs. 2 and 3. The simulation videos can be found in Supplementary Video SV7.

4. Discussion

An individual NV in solids tends to minimize its total surface energy γ for a specific volume and thus often has a polyhedral shape with low-indexed crystallographic facets [59]. Thermodynamically, the equilibrium shape of a NV should satisfy the minimum-energy condition that can be described by the Wulff construction (γ plot) [60,61]. However, the NVs formed in Cu during magnetron sputtering could exhibit a more complex shape, since sputtering is a nonequilibrium deposition process [62]. NVs have been observed in several sputtered metallic thin films, and their morphology and distribution are likely to be influenced by apparatus geometry and deposition conditions [63–65]. In the current study, the introduced NVs in sputtered Cu film are primarily faceted on {111} planes and elongated along <112> direction, as shown in Fig. 1. The *in situ* TEM observations in Figs. 2 and 3 demonstrate that high-temperature heavy-ion irradiations led to the geometry change of such faceted and elongated NVs in two aspects: spheroidization (shape change) and shrinkage (size change). Furthermore, smaller and spherical voids were able to migrate when irradiated at 350 °C.

4.1. Void spheroidization and shrinkage

It has been found that the elongated NVs tend to become spherical under high-temperature irradiation environments. As shown in Fig. 5(a), the void aspect ratio μ increases through the reduction of void length L and the concurrent expansion of width W. The spheroidization may be caused by two factors: surface migration and diffusion, driven by local curvature (surface tension) and surface energy anisotropy, respectively. Meanwhile, the NVs kept shrinking as shown in Fig. 3. During irradiation, even though an equal number of vacancies and interstitials are created at the same time, many vacancies are stored in SFTs (see Fig. 8) that are im-

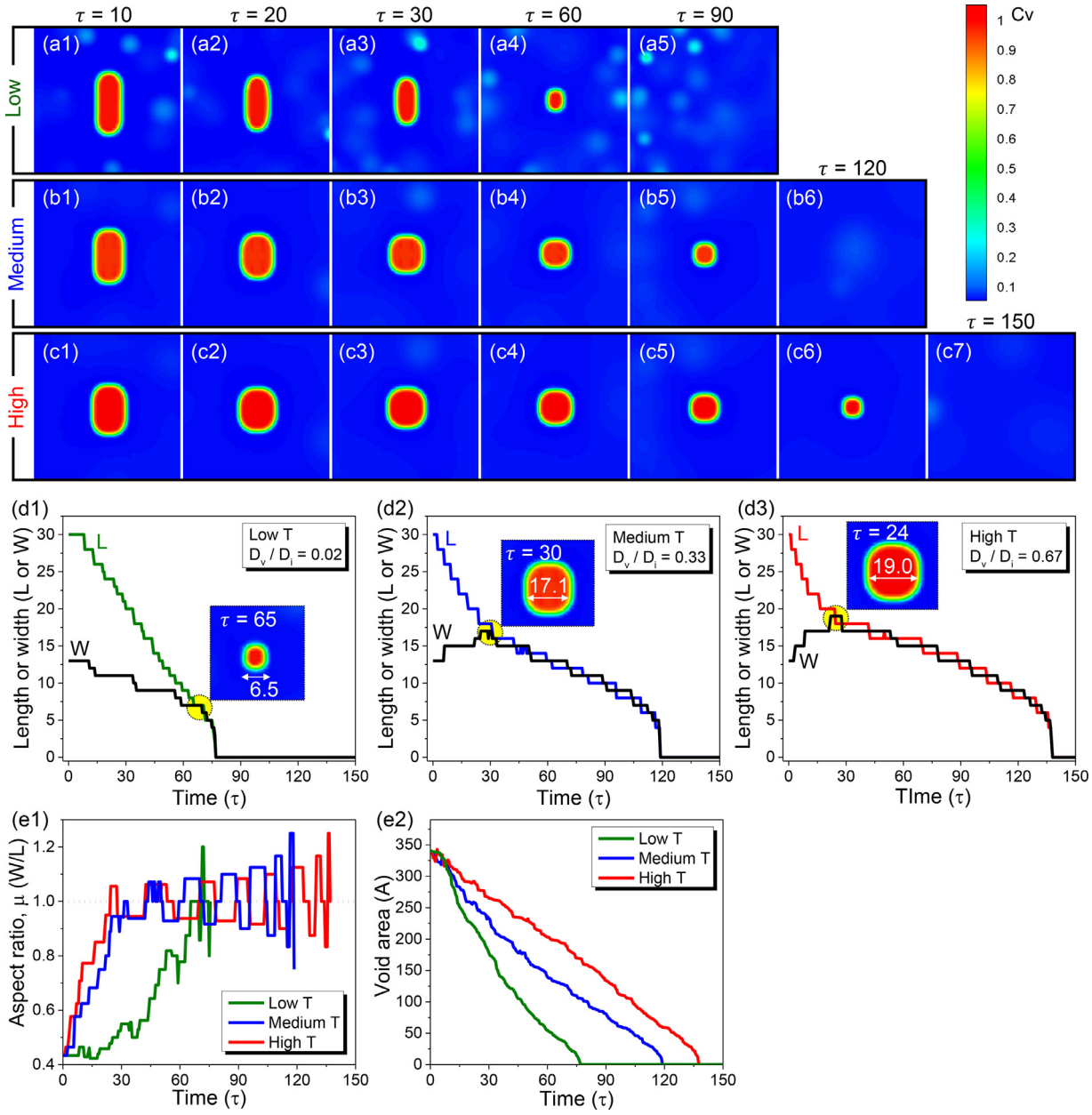

Fig. 10. Phase field simulations on the irradiation-induced void spheroidization and shrinkage. The interstitial diffusivity D_i is kept as a constant of 60 for all three cases, while the vacancy diffusivity D_v is set as 1 for the low temperature in (a1)-(a5), 20 for the medium temperature in (b1)-(b6), and 40 for the high temperature in (c1)-(c7). (d1)-(d3) The evolution of void length (L) and width (W). (e1) and (e2) Temperature effect on variations of void aspect ratio (W/L) and void area (A). The corresponding videos can be found in Supplementary Video SV7.

mobile 3D vacancy clusters and unable to interact with preexisting NVs. Hence the void shrinkage is attributed to the net flux of interstitials into the NVs. Also compared with vacancies, interstitials have greater diffusivity due to their lower migration energy barrier [25]. Taking into consideration of above defect bias, our modified phase field modeling in Fig. 10 shows the same trend of void shrinkage as observed during *in situ* TEM irradiations. The biased cascades in the simulation qualitatively modeled the effects of SFTs on the void evolution. Recent molecular dynamics simulation studies also demonstrated that radiation can induce void shrinkage when atomic displacements occur in the vicinity of NVs, plausibly due to a biased formation of vacancies and their emissions away from NVs [66,67].

It is worth pointing out that the specimen used for *in situ* TEM experiment is approximately 100 nm in thickness, so the foil free surfaces, top or bottom, shall play an important role in absorbing point defects and affect void shrinkage or swelling. Unlike dislocations that are interstitial biased sinks, free surfaces are classified as neutral (or unbiased) sinks that absorb both interstitials and vacancies [68,69]. On the free surfaces of TEM foil, the vacancy concentration is assumed to be thermally in equilibrium C_v^0. On the NV surface, however, the vacancy concentration C_v^V is related to the surface curvature and given by [70]:

$$C_v^V = C_v^0 \exp\left(\frac{2\gamma\Omega}{RkT}\right) \tag{5}$$

where γ is free surface energy, Ω is atomic volume, R is void radius, k is Boltzmann's constant, and T is temperature. Eq. (5) suggests that the equilibrium vacancy concentration on the TEM foil surface is lower than that on the void surface. In other words, the

foil surfaces can counterbalance more vacancies and facilitate void shrinkage rather than swelling. In addition, Eq. (5) also suggests that the NVs would gradually emit vacancies and eventually evaporate at high temperature even without irradiation. The vacancy emission rate $\dot{R}_v$ can be described by [71]:

$$\dot{R}_v = \frac{D_v C_v^0}{R}\left[1 - \exp\left(\frac{2\Omega\gamma}{kTR}\right)\right] \quad (6)$$

Using Eq. (6), the predictions of $\dot{R}_v$ at 250 °C and 350 °C are plotted in Supplementary Figure S3, together with the experimentally measured data points. It shows that the thermal evaporation is negligible for the large voids (> 5 nm in diameter) of interest. Therefore, the void shrinkage observed in the current study is primarily caused by the heavy ion irradiation effect.

Fig. 5(b) and (d) show that the rates of spheroidization and shrinkage are higher for smaller NVs. With decreasing void size, the driving force of curvature for surface mobility increases, so the spheroidization is accelerated for smaller NVs. In our previous work [49], we demonstrated the effects of curvature on the spherodization rate using the phase-field approach by simulating the evolution of two voids that vastly differ in size. In addition, as the void shrinkage originates from the net flux of interstitials, the common form of the void growth rate $\dot{R}$ is given by [25]:

$$\dot{R} = \frac{\Omega}{R}\left[D_i C_i - D_v(C_v - C_v^V)\right] \quad (7)$$

where D_i and D_v are interstitial and vacancy diffusivity, C_i and C_v are interstitial and vacancy concentration in the solid, and Ω, R and C_v^V are the same parameters defined in Eq. (5). Combining Eqs. (5) and (7), it is concluded that the shrinkage rate of NVs increases with decreasing void radius R, consistent with our *in situ* observations and previous reports [72,73].

4.2. Void migration

The migrations of irradiation-induced defect clusters, two- or three-dimensional in configuration, could have profound impact on the evolutions of material microstructure and property [50,74]. It has been long known that the two-dimensional defect clusters, such as interstitial loops, are highly mobile [74,75]. Unlike individual point defects that diffuse by means of random atomic jump, the dislocation loops migrate along certain crystallographic orientations, and their mobility is closely associated with cluster configuration, lattice structure, habit plane, Burgers vector, and the local environment [75–81]. For instance, a perfect loop can exhibit fast one-dimensional migration under radiation, and it moves along a certain direction parallel to its Burgers vector, driven by the collective motion of numerous neighboring atoms in the loop [75,82,83]. In addition, molecular dynamics simulations reveal that the mobility of dislocation loops strongly depends on the loop size and decreases significantly as the loop size approaches that of dislocation lines in unirradiated materials [84]. In contrast, the three-dimensional defect clusters, including SFTs and voids, are assumed to be extremely difficult to diffuse through crystalline lattice. For instance, SFTs are regarded as immobile clusters and no experimental evidence has ever been reported on their mobility [85]. However, NVs are predicted to be mobile in the presence of thermal gradient, which accounts for the formation of holes and intragranular bubbles in nuclear fuels [86–88]. Recently, a couple of phase-field simulation studies have been reported regarding the migration behaviors of NVs under gradient temperature field [89–94]. According to one of the studies, the void velocity v caused by thermal gradient is described by [89]:

$$v = C_0 + \frac{C}{D} \quad (8)$$

Note that the Eq. (8) is quite different from our statistic result in Eq. (2), as it takes no consideration of irradiation environment. In our case, the thin TEM foil was heated to 350 °C, and it remained an isothermal state during irradiation, so there was no long-range temperature gradient throughout the sample. Moreover, we found that the voids apparently stopped moving without Kr ion beam. As such, we speculate that the void migration may result from the interaction of NVs with radiation cascades.

The damage cascade is normally pictured as a displacement spike with a high 'hot' vacancy core surrounded by a 'cold' interstitial shell [95]. Its local field is thus largely out of equilibrium because of thermal and concentration gradients in a radial direction from core to shell. When a cascade occurs closely to a void, the extra interstitials on the cascade shell would diffuse into the void and lead to void shrinkage. Meanwhile, the vacancy-rich core might collapse into an SFT [96,97]. This speculation is supported by three evidence. First, for the 1 MeV Kr^{++} irradiation in Cu, the damage cascade size is estimated to be ~ 7 nm [98], comparable to the critical size for a void to migrate observed experimentally. The voids with diameters much larger than cascade hardly migrate as the local driving force of thermal and concentration gradients are too low. Second, the irradiation-induced SFTs have edge lengths of 1 to 7 nm (see Fig. 8), slightly smaller than the cascade size. The locations of these immobile SFTs are likely to be where the cascades took place during irradiation. Third, the small mobile voids tend to follow a random walk in any directions (Fig. 7c), which is analogous to the random Brownian motion of small particles in fluid due to their collision with fast-moving molecules. Similarly, the migration of small voids in solids might result from their interaction with local damage cascades.

4.3. Irradiation temperature effect on void evolution

Our experiments and simulations reveal that the void spheroidization and shrinkage are largely influenced by irradiation temperature. First, at higher temperature, the surface migration and diffusion of point defects increase, so the void spheroidization is assumed to be accelerated with increasing temperature. This hypothesis agrees with our *in situ* TEM observations in Fig. 2 and is well explained by our phase field simulations in Fig. 10. The surface diffusion of atoms is built into the phase-field model through the mobility function, Eq. (9), of the point defects which also allows for the bulk diffusion in the matrix. The simulations reported in Fig. 10 clearly indicate the spheroidization and its rate dependence on the temperature. It is evident from Eq. (9) that increasing the diffusivity of vacancies enhances the surface mobility of atoms and thus verifying the mechanism for spheroidization and its rate dependence on temperature.

$$M_\alpha = D_\alpha C_\alpha (1 - C_v - C_i) \quad (9)$$

In particular, at 250 °C the irradiated and fully spheroidized NVs still exhibited craters from time to time, as shown in Fig. 4. This phenomenon must be related to the interaction between radiation cascades and pre-existing NVs. To support this assumption, another phase field simulation was conducted, and the simulation results are summarized in Fig. 11. In this case, we set the ratio of the point diffusivities, D_v/D_i, to 0.2. Fig. 11(a) illustrates the initial shape and size of a perfect circular void in two dimensions, and the white crosses mark 4 fixed locations of damage cascades nearby. With increasing dose, it is evident that the circular void experiences local curvature variations, as marked by the arrows in Fig. 11(c) and (d). In the meantime, the void keeps shrinking. When $\tau = 200$ in Fig. 11(d), the void diameter has reduced from 16.0 to 12.2. The simulation video can be found in Supplementary Video SV8.

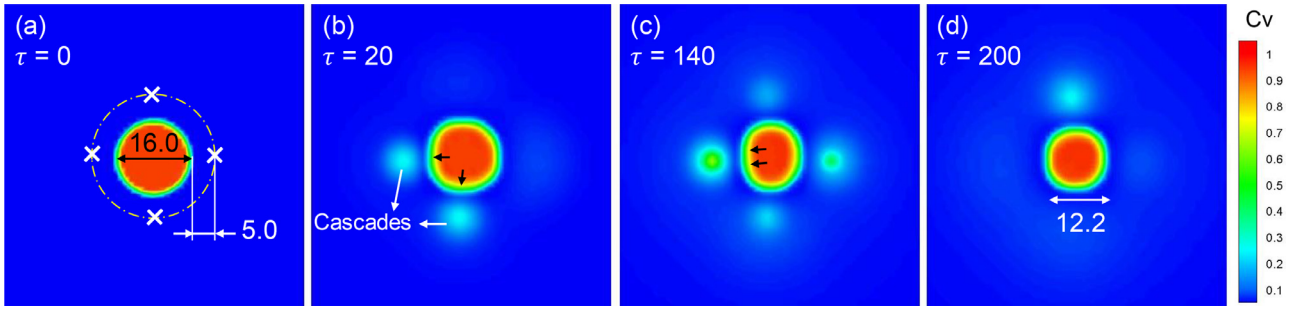

Fig. 11. Phase field modeling on the surface curvature change for a nearly perfect spherical void, caused by radiation cascades nearby. (a) When $\tau = 0$, the introduced void has a perfect circular shape with an initial diameter of 16. Four cascades were placed symmetrically at a larger concentric circle, 5 units away from the void surface, as marked by the white crosses. (b)-(d) With increasing time, the void surface changes locally, and void size decreases, due to the on-going cascades. The corresponding video can be found in Supplementary Video SV8.

On the other hand, with increasing temperature the vacancy diffusivity increases, so more interstitials will be consumed through point-defect recombination before they can diffuse into NVs. As a result, the NV shrinkage process recedes at a higher radiation temperature, as demonstrated in Fig. 5(c). This phenomenon is also inferred by the drop of remaining vacancy concentration (stored in SFTs) in irradiated specimens with increasing temperature as shown in Fig. 8(e). Phase-field simulations were performed to confirm the hypothesized mechanism for the shrinkage rate dependence on temperature. By varying the ratio of point defect diffusivities, we studied the temperature effects on the void evolution. The ratios chosen for point defect diffusivities emulate the working temperatures in the experiments. By keeping the cascade nucleation profile and initial size of the void same across the simulations, we verified the hypothesis for shrinkage rate dependence on temperature. Increased recombination reactions due to enhanced vacancy diffusivity relative to interstitials is indeed the reason for the reduction in shrinkage rate of voids at elevated temperatures.

Furthermore, for the Cu irradiated by neutrons, its peak swelling occurs at ~ 325 °C [3]. However, no void nucleation and growth were observed in the current heavy ion irradiation study. This discrepancy is partially because of the TEM foil surface effect discussed above, and partially because of the peak swelling temperature shift to a higher value due to the heavy ion irradiation effect [99]. In contrast to the low dose rate (~ 10^{-8} dap/s) of neutron irradiation, the damage date in ion irradiation is usually 3–5 orders of magnitude higher (~ 3×10^{-4} dap/s in current case) [100]. The higher dose rate increases defect production rate; meanwhile, it also increases the defect recombination rate. As a result, to achieve the similar result of neutron irradiation, the ion irradiation requires an increase in temperature to enhance the defect migration rate, so it can ensure equivalent portion of survival defects [18]. We speculate that the void swelling could occur if the irradiation temperature increases further, but an incubation period might be required to initiate such swelling.

4.4. Irradiation temperature effect on SFTs

The post-irradiation analysis in Fig. 8 reveals that the residual defect clusters are dominated by SFTs, a type of 3D vacancy clusters that usually form in face-centered-cubic (FCC) metals with low stacking fault energies [57,101,102], driven by vacancy supersaturation under various conditions, such as quenching and aging [103], high-speed deformation [104], or radiation damage [55,105]. In Cu, it has been demonstrated that SFTs are much more stable than other defects, such as voids and dislocation loops (perfect or faulted), because of their low formation energies [57]. Prior studies showed that the irradiation-induced SFTs in Cu are typically < 8 nm in edge length [101], and can rapidly reach a saturation number density of ~ 5×10^{23} m^{-3} at a low dose, ~ 0.1 dpa [106], which is consistent with our observations in Fig. 8(a)-(c).

In addition, our systematic studies in Fig. 8(d) and (e) reveal that the SFT size increases with increasing temperature, whereas the SFT density evolves in the opposite way. Such temperature-dependent evolution must be strongly associated with SFT formation process. Unfortunately, a direct observation of the process is experimentally difficult due to spatial resolution and time limitation [96,107]. To date, although it is widely accepted that SFTs arise from the clustering of vacancies, the kinetics of their formation mechanism remains unclear [107–110]. Several potential formation mechanisms have been proposed based on theoretical analyses or computer simulations, according to which SFTs could be formed through the aggregation of individual vacancies [109], dissociation of Frank loops [103,111,112], transformation of voids [96], or direct collapse of radiation cascades [97,113]. Moreover, it was also reported that SFTs can form through the interaction of partial dislocations in the deformed nanocrystalline Au, even when vacancies are scanty [114]. In summary, these studies indicate that SFTs are energetically favorable defect configurations and they can form and remain stable under various extreme environments. In this work, we attempt to understand the influence of irradiation temperature on SFT size and density from the cascade model [97,113]. This model suggests that SFTs result from the solidifications of displacement cascade core that is depleted in mass and is often vacancy-rich in a liquid-like (or quasi-molten) state [115,116]. It is assumed that the cascade periphery is abundant with interstitials that are highly mobile and can escape from the core region through thermal diffusion. When temperature increases, the vacancy core expands and gets closer to the interstitial periphery [117]. Therefore, smaller SFTs are expected to be removed through the core-interstitial recombination at higher radiation temperatures. Consequently, the SFT density decreases while the SFT size increases with increasing temperature, in agreement with our observations shown in Fig. 8.

5. Conclusions

In situ TEM Kr ion irradiation was combined with phase field simulation to examine the irradiation-induced void spheroidization, shrinkage and migration in highly textured Cu (110) films with NVs. Void spheroidization is accomplished via surface point-defect migration and diffusion, driven by surface tension and anisotropy energy. The void shrinkage is a result of net interstitial flux into NVs. Void migration is more dramatic for smaller NVs (< 6.5 nm in diameter) and follows a random walk pattern. The void migration may be driven by damage cascade induced point defect concentration gradient. Increasing irradiation temperature can fa-

cilitate spheroidization but impede void shrinkage; can decrease the SFT density, but increase the SFT size, presumably because of the accelerated recombination between cascade core and interstitial rich periphery.

Declaration of Competing Interest

The authors declare that they have no known competing financial interests or personal relationships that could have appeared to influence the work reported in this paper.

Acknowledgments

We acknowledge financial support by NSF-CMMI-1728419. Suncai Fan was also supported by the Bilsland Dissertation Fellowship at Purdue University. Zhongxia Shang was supported by NSF-DMR-Metallic Materials and Nanostructures Program under grant 1611380. Haiyan Wang acknowledges the support from the U.S. Office of Naval Research (N00014–16–1–2778). Work at the IVEM-Tandem Facility, ANL was supported by the U.S. Department of Energy, Office of Nuclear Energy under DOE Idaho Operations Office Contract DE-AC07- 051D14517 as part of a Nuclear Science User Facilities experiment.

Supplementary materials

Supplementary material associated with this article can be found, in the online version, at doi:10.1016/j.actamat.2020.10.008.

References

[1] C. Cawthorne, E. Fulton, Voids in irradiated stainless steel, Nature 216 (5115) (1967) 575–576.
[2] J. Evans, Void swelling and irradiation-induced void shrinkage in neutron irradiated molybdenum and TZM, J. Nucl. Mater. 88 (1) (1980) 31–41.
[3] S.J. Zinkle, K. Farrell, Void swelling and defect cluster formation in reactor-irradiated copper, J. Nucl. Mater. 168 (3) (1989) 262–267.
[4] E. Little, D. Stow, Void-swelling in irons and ferritic steels: II. An experimental survey of materials irradiated in a fast reactor, J. Nucl. Mater. 87 (1) (1979) 25–39.
[5] C. Dennett, K. So, A. Kushima, D. Buller, K. Hattar, M. Short, Detecting self-ion irradiation-induced void swelling in pure copper using transient grating spectroscopy, Acta Mater 145 (2018) 496–503.
[6] T. LaGrange, K. Arakawa, H. Yasuda, M. Kumar, Preferential void formation at crystallographically ordered grain boundaries in nanotwinned copper thin films, Acta Mater 96 (2015) 284–291.
[7] I. Ipatova, R. Harrison, S. Donnelly, M. Rushton, S. Middleburgh, E. Jimenez-Metere, Void evolution in tungsten and tungsten-5 wt.% tantalum under in-situ proton irradiation at 800 and 1000 °C, J. Nucl. Mater. (2019).
[8] R. Rau, R. Ladd, J. Moteff, Voids in Irradiated Tungsten and Molybdenum, General Electric Co., Cincinnati, Ohio, 1969 Missile and Space Div..
[9] X. Wang, A.M. Monterrosa, F. Zhang, H. Huang, Q. Yan, Z. Jiao, G.S. Was, L. Wang, Void swelling in high dose ion-irradiated reduced activation ferritic–martensitic steels, J. Nucl. Mater. 462 (2015) 119–125.
[10] E. Getto, K. Sun, A. Monterrosa, Z. Jiao, M. Hackett, G. Was, Void swelling and microstructure evolution at very high damage level in self-ion irradiated ferritic-martensitic steels, J. Nucl. Mater. 480 (2016) 159–176.
[11] D. Gelles, Void swelling in binary FeCr alloys at 200 dpa, J. nucl. mater. 225 (1995) 163–174.
[12] J. Straalsund, R. Powell, B. Chin, An overview of neutron irradiation effects in LMFBR materials, J. Nucl. Mater. 108 (1982).
[13] M.B. Toloczko, F. Garner, V. Voyevodin, V. Bryk, O. Borodin, V. Mel'Nychenko, A. Kalchenko, Ion-induced swelling of ODS ferritic alloy MA957 tubing to 500 dpa, J. Nucl. Mater. 453 (1–3) (2014) 323–333.
[14] D.L. Porter, F.A. Garner, Irradiation creep and embrittlement behavior of AISI 316 stainless steel at very high neutron fluences, J. Nucl. Mater. 159 (1988) 114–121.
[15] J. Knapp, D. Follstaedt, S. Myers, Hardening by bubbles in He-implanted Ni, J Appl Phys 103 (1) (2008) 013518.
[16] S. Porollo, A. Dvoriashin, A. Vorobyev, Y.V. Konobeev, The microstructure and tensile properties of Fe–Cr alloys after neutron irradiation at 400 C to 5.5–7.1 dpa, J. nucl. mater. 256 (2–3) (1998) 247–253.
[17] S.J. Zinkle, J.T. Busby, Structural materials for fission & fusion energy, Mater. today 12 (11) (2009) 12–19.
[18] G.S. Was, Challenges to the use of ion irradiation for emulating reactor irradiation, J Mater Res 30 (9) (2015) 1158.
[19] P. Goodhew, Shapes of pores in metals, Metal Sci. 15 (9) (1981) 377–385.
[20] M.R. Mruzik, K.C. Russell, Equilibrium forms of small voids in metals, Surf Sci 67 (1) (1977) 205–225.
[21] C. Chen, The shapes of irradiation-produced voids in nickel, physica status solidi (a) 16 (1) (1973) 197–210.
[22] P.C. Millett, A. El-Azab, S. Rokkam, M. Tonks, D. Wolf, Phase-field simulation of irradiated metals: part I: void kinetics, Comput. mater. sci. 50 (3) (2011) 949–959.
[23] A. Brailsford, R. Bullough, The rate theory of swelling due to void growth in irradiated metals, J. Nucl. Mater. 44 (2) (1972) 121–135.
[24] S. Zinkle, K. Farrell, H. Kanazawa, Microstructure and cavity swelling in reactor-irradiated dilute copper-boron alloy, J. nucl. mater. 179 (1991) 994–997.
[25] G.S. Was, Fundamentals of Radiation Materials science: Metals and Alloys, Springer, 2016.
[26] K. Niwase, T. Ezawa, F. Fujita, H. Kusanagi, H. Takaku, Morphology of micro–cavities in nickel during helium bombardment and post-irradiation annealing, Radiat Eff 106 (1–2) (1988) 65–76.
[27] S. Kondo, Y. Katoh, L.L. Snead, Unidirectional formation of tetrahedral voids in irradiated silicon carbide, Appl Phys Lett 93 (16) (2008) 163110.
[28] S. Zinkle, B. Singh, Microstructure of Cu–Ni alloys neutron irradiated at 210 °C and 420 °C to 14 dpa, J. nucl. mater. 283 (2000) 306–312.
[29] K. Farrell, J. Houston, Suppression of radiation damage microstructure in aluminum by trace impurities, J. Nucl. Mater. 83 (1) (1979) 57–66.
[30] W. Xu, Y. Zhang, G. Cheng, W. Jian, P.C. Millett, C.C. Koch, S.N. Mathaudhu, Y. Zhu, In-situ atomic-scale observation of irradiation-induced void formation, Nat Commun 4 (2013) 2288.
[31] A. Bhattacharya, E. Meslin, J. Henry, B. Décamps, A. Barbu, Dramatic reduction of void swelling by helium in ion-irradiated high purity α-iron, Mater. Res. Lett. 6 (7) (2018) 372–377.
[32] P. Maziasz, Formation and stability of radiation-induced phases in neutron-irradiated austenitic and ferritic steels, J. Nucl. Mater. 169 (1989) 95–115.
[33] J.L. Katz, H. Wiedersich, Effect of insoluble gas molecules on nucleation of voids in materials supersaturated with both vacancies and interstitials, J. Nucl. Mater. 46 (1) (1973) 41–45.
[34] A. Bhattacharya, E. Meslin, J. Henry, A. Barbu, S. Poissonnet, B. Décamps, Effect of chromium on void swelling in ion irradiated high purity Fe–Cr alloys, Acta Mater 108 (2016) 241–251.
[35] H. Brager, The effects of cold working and pre-irradiation heat treatment on void formation in neutron-irradiated type 316 stainless steel, J. Nucl. Mater. 57 (1) (1975) 103–118.
[36] L. Mansur, Correlation of neutron and heavy-ion damage: II. The predicted temperature shift if swelling with changes in radiation dose rate, J. Nucl. Mater. 78 (1) (1978) 156–160.
[37] A. Brailsford, R. Bullough, The stress dependence of high temperature swelling, J. Nucl. Mater. 48 (2) (1973) 87–106.
[38] D.R. Olander, Fundamental Aspects of Nuclear Reactor Fuel elements: Solutions to Problems, California Univ., BerkeleyUSA, 1976 Dept. of Nuclear Engineering.
[39] A. Brailsford, L. Mansur, Time dependent rate theory for diffusional defect processes, Acta Metall. 33 (8) (1985) 1425–1437.
[40] L. Mansur, Theory and experimental background on dimensional changes in irradiated alloys, J. Nucl. Mater. 216 (1994) 97–123.
[41] N.M. Ghoniem, Clustering theory of atomic defects, Radiation effects and defects in solids 148 (1–4) (1999) 269–318.
[42] H. Wiedersich, Theory of Defect Clustering and Void Formation, Argonne National Lab., Ill.(USA), 1975.
[43] L.-.Q. Chen, Phase-field models for microstructure evolution, Annu Rev Mater Res 32 (1) (2002) 113–140.
[44] S. Rokkam, A. El-Azab, P. Millett, D. Wolf, Phase field modeling of void nucleation and growth in irradiated metals, Modell. and simul. mater. sci. eng. 17 (6) (2009) 064002.
[45] P.C. Millett, S. Rokkam, A. El-Azab, M. Tonks, D. Wolf, Void nucleation and growth in irradiated polycrystalline metals: a phase-field model, Model simul mater. sci. eng. 17 (6) (2009) 064003.
[46] P.C. Millett, A. El-Azab, D. Wolf, Phase-field simulation of irradiated metals: part II: gas bubble kinetics, Comput. Mater Sci. 50 (3) (2011) 960–970.
[47] W. Liu, N. Wang, Y. Ji, P. Song, C. Zhang, Z. Yang, L. Chen, Effects of surface energy anisotropy on void evolution during irradiation: a phase-field model, J. Nucl. Mater. 479 (2016) 316–322.
[48] Z. Xiao, A. Semenov, C. Woo, S. Shi, Single void dynamics in phase field modeling, J. Nucl. Mater. 439 (1) (2013) 25–32.
[49] C. Fan, A. Sreekar, Z. Shang, J. Li, M. Li, H. Wang, A. El-Azab, X. Zhang, Radiation induced nanovoid shrinkage in Cu at room temperature: an *in situ* study, Scr Mater 166 (2019) 112–116.
[50] S. Zinkle, 1.03-Radiation-Induced effects on microstructure, Compr. nucl. mater. 1 (2012) 65–98.
[51] J.F. Ziegler, M.D. Ziegler, J.P. Biersack, SRIM–The stopping and range of ions in matter, Nuclear Instruments and Methods in Physics Research Section B: Beam Interactions with Materials and Atoms 268 (11–12) (2010) 1818–1823.
[52] R.E. Stoller, M.B. Toloczko, G.S. Was, A.G. Certain, S. Dwaraknath, F.A. Garner, On the use of SRIM for computing radiation damage exposure, Nuclear instruments and methods in physics research section B: beam interactions with materials and atoms 310 (2013) 75–80.
[53] Y. Chen, K.Y. Yu, Y. Liu, S. Shao, H. Wang, M. Kirk, J. Wang, X. Zhang, Damage–tolerant nanotwinned metals with nanovoids under radiation environments, Nat Commun 6 (2015).

[54] D.B. Williams, C.B. Carter, in: The Transmission Electron microscope, Transmission electron Microscopy, Springer, 1996, pp. 3–17.
[55] R. Schäublin*, Z. Yao, N. Baluc, M. Victoria, Irradiation-induced stacking fault tetrahedra in fcc metals, Philos. mag. 85 (4–7) (2005) 769–777.
[56] S. Zinkle, R. Sindelar, Defect microstructures in neutron-irradiated copper and stainless steel, J. Nucl. Mater. 155 (1988) 1196–1200.
[57] S. Zinkle, L. Seitzman, W. Wolfer I, Energy calculations for pure metals, Philos. Mag. A 55 (1) (1987) 111–125.
[58] A. El-Azab, K. Ahmed, S. Rokkam, T. Hochrainer, Diffuse interface modeling of void growth in irradiated materials, Mathematical, thermodynamic and atomistic perspectives, Current opinion in solid state and materials science 18 (2) (2014) 90–98.
[59] R. Nelson, D. Mazey, R. Barnes, The thermal equilibrium shape and size of holes in solids, Philos. Mag. 11 (109) (1965) 91–111.
[60] J.W. Christian, The Theory of Transformations in Metals and Alloys, Newnes, 2002.
[61] D.A. Porter, K.E. Easterling, M. Sherif, Phase Transformations in Metals and Alloys, (Revised Reprint), CRC press, 2009.
[62] I. Petrov, P. Barna, L. Hultman, J. Greene, Microstructural evolution during film growth, J Vac. Sci. Technol A: Vac, Surf., Films 21 (5) (2003) S117–S128.
[63] K.H. Müller, A computer model for postdeposition annealing of porous thin films, J Vac. Sci. Technol A: Vac, Surf, and Films 3 (6) (1985) 2089–2092.
[64] A. Haghiri-Gosnet, F. Ladan, C. Mayeux, H. Launois, M. Joncour, Stress and microstructure in tungsten sputtered thin films, J Vac Sci Technol A: Vac., Surf., and Films 7 (4) (1989) 2663–2669.
[65] J.A. Thornton, Influence of apparatus geometry and deposition conditions on the structure and topography of thick sputtered coatings, J. Vac Sci. Technol. 11 (4) (1974) 666–670.
[66] N. Lazarev, V. Dubinko, Molecular dynamics simulation of defects production in the vicinity of voids, Radiat. eff. defects in solids 158 (11–12) (2003) 803–810.
[67] V. Dubinko, N. Lazarev, Effect of the radiation-induced vacancy emission from voids on the void evolution, Nucl. Instrum. and Methods in Phys. Res. Sec. B: Beam Interac. Mater. and Atoms 228 (1–4) (2005) 187–192.
[68] C. Woo, B. Singh, Production bias due to clustering of point defects in irradiation-induced cascades, Philos. Mag. A 65 (4) (1992) 889–912.
[69] N. Doan, G. Martin, Elimination of irradiation point defects in crystalline solids: sink strengths, Phys. Rev. B 67 (13) (2003) 134107.
[70] T. Hochrainer, A. El-Azab, A sharp interface model for void growth in irradiated materials, Philos. Mag. 95 (9) (2015) 948–972.
[71] V. Sears, Kinetics of void growth in irradiated metals, J. Nucl. Mater. 39 (1) (1971) 18–26.
[72] J. Fikus, R. Johnson, Effect of surface energy barriers on void growth kinetics, Radiat Eff 40 (1–2) (1979) 63–70.
[73] N. Packan, D. Braski, Electron microscope *in situ* annealing study of voids induced by irradiation in aluminum, J. Nucl. Mater. 34 (3) (1970) 307–314.
[74] C. Lu, L. Niu, N. Chen, K. Jin, T. Yang, P. Xiu, Y. Zhang, F. Gao, H. Bei, S. Shi, Enhancing radiation tolerance by controlling defect mobility and migration pathways in multicomponent single-phase alloys, Nat Commun 7 (2016) 13564.
[75] K. Arakawa, K. Ono, M. Isshiki, K. Mimura, M. Uchikoshi, H. Mori, Observation of the one-dimensional diffusion of nanometer-sized dislocation loops, Science 318 (5852) (2007) 956–959.
[76] Y. Matsukawa, S.J. Zinkle, One-dimensional fast migration of vacancy clusters in metals, Science 318 (5852) (2007) 959–962.
[77] H. Abe, N. Sekimura, Y. Yang, Stability and mobility of defect clusters in copper under displacement cascade conditions, J. nucl. mater. 323 (2–3) (2003) 220–228.
[78] H. Abe, N. Sekimura, T. Tadokoro, Stability and mobility of interstitial-type defect clusters generated from displacement cascades in copper and gold by in-situ transmission electron microscopy, Mater. trans. 46 (3) (2005) 433–439.
[79] K. Arakawa, K. Ono, H. Mori, A.S. Avilov, S.L. Dudarev, L.D. Marks, In-Situ Transmission Electron Microscopy of the Dynamics of Point-Defect Clusters in Metals, in: AIP Conference Proceedings, AIP, 2008, pp. 66–78.
[80] K. Arakawa, M. Hatanaka, E. Kuramoto, K. Ono, H. Mori, Changes in the Burgers vector of perfect dislocation loops without contact with the external dislocations, Phys. Rev. Lett. 96 (12) (2006) 125506.
[81] D. Hull, D.J. Bacon, Introduction to Dislocations, Butterworth-Heinemann, 2001.
[82] K. Arakawa, M. Hatanaka, H. Mori, K. Ono, Effects of chromium on the one-dimensional motion of interstitial-type dislocation loops in iron, J. nucl. mater. 329 (2004) 1194–1198.
[83] M. Kiritani, Defect interaction processes controlling the accumulation of defects produced by high energy recoils, J. nucl. mater. 251 (1997) 237–251.
[84] Y.N. Osetsky, D. Bacon, A. Serra, B. Singh, S. Golubov, Stability and mobility of defect clusters and dislocation loops in metals, J. Nucl. Mater. 276 (1–3) (2000) 65–77.
[85] Y. Matsukawa, S.J. Zinkle, Dynamic observation of the collapse process of a stacking fault tetrahedron by moving dislocations, J. Nucl. Mater. 329 (2004) 919–923.
[86] S. Kashibe, K. Une, K. Nogita, Formation and growth of intragranular fission gas bubbles in UO2 fuels with burnup of 6–83 GWd/t, J. nucl. mater. 206 (1) (1993) 22–34.
[87] I. Zacharie, S. Lansiart, P. Combette, M. Trotabas, M. Coster, M. Groos, Microstructural analysis and modelling of intergranular swelling of an irradiated UO2 fuel treated at high temperature, J. nucl. mater. 255 (2–3) (1998) 92–104.
[88] K. Katsuyama, T. Nagamine, S.-i. Matsumoto, M. Ito, Measurement of central void diameter in FBR MOX fuel by X-ray computer tomography, J Nucl Sci Technol 39 (7) (2002) 804–806.
[89] S.Y. Hu, C. Henager Jr., Phase-field simulation of void migration in a temperature gradient, Acta Mater 58 (9) (2010) 3230–3237.
[90] W. Chen, Y. Peng, X.a. Li, K. Chen, J. Ma, L. Wei, B. Wang, Y. Zheng, Phase-field study on geometry-dependent migration behavior of voids under temperature gradient in UO2 crystal matrix, J Appl Phys 122 (15) (2017) 154102.
[91] I.W. Vance, P.C. Millett, Phase-field simulations of pore migration and morphology change in thermal gradients, J. Nucl. Mater. 490 (2017) 299–304.
[92] S. Biner, Pore and grain boundary migration under a temperature gradient: a phase-field model study, Modell. Simul. Mater. Sci. Eng. 24 (3) (2016) 035019.
[93] L. Zhang, M.R. Tonks, P.C. Millett, Y. Zhang, K. Chockalingam, B. Biner, Phase–field modeling of temperature gradient driven pore migration coupling with thermal conduction, Comput. Mater. Sci. 56 (2012) 161–165.
[94] Y. Li, S. Hu, X. Sun, F. Gao, C.H. Henager Jr., M. Khaleel, Phase-field modeling of void migration and growth kinetics in materials under irradiation and temperature field, J. Nucl. Mater. 407 (2) (2010) 119–125.
[95] J.A. Brinkman, Production of atomic displacements by high-energy particles, Am J Phys 24 (4) (1956) 246–267.
[96] B. Uberuaga, R. Hoagland, A. Voter, S. Valone, Direct transformation of vacancy voids to stacking fault tetrahedra, Phys. Rev. Lett. 99 (13) (2007) 135501.
[97] Y.N. Osetsky, D. Bacon, Defect cluster formation in displacement cascades in copper, Nuclear Inst. Methods in Phys. Res. Sec. B: Beam Interact. with Mater. Atoms 180 (1–4) (2001) 85–90.
[98] C. Fan, Z. Shang, T. Niu, J. Li, H. Wang, X. Zhang, Dual Beam In Situ Radiation Studies of Nanocrystalline Cu, Materials (Basel) 12 (17) (2019) 2721.
[99] N. Packan, K. Farrell, J. Stiegler, Correlation of neutron and heavy-ion damage: I. The influence of dose rate and injected helium on swelling in pure nickel, J. Nucl. Mater. 78 (1) (1978) 143–155.
[100] G.S. Was, T. Allen, Intercomparison of microchemical evolution under various types of particle irradiation, (1993).
[101] B.N. Singh, S.I. Golubov, H. Trinkaus, D.J. Edwards, M. Eldrup, Evolution of stacking fault tetrahedra and its role in defect accumulation under cascade damage conditions, J. Nucl. Mater. 328 (2–3) (2004) 77–87.
[102] D.J. Edwards, E.P. Simonen, S.M. Bruemmer, Evolution of fine-scale defects in stainless steels neutron-irradiated at 275 C, J. nucl. mater. 317 (1) (2003) 13–31.
[103] J. Silcox, P. Hirsch, Direct observations of defects in quenched gold, Philos. Mag. 4 (37) (1959) 72–89.
[104] M. Kiritani, Y. Satoh, Y. Kizuka, K. Arakawa, Y. Ogasawara, S. Arai, Y. Shimomura, Anomalous production of vacancy clusters and the possibility of plastic deformation of crystalline metals without dislocations, Philos Mag Lett 79 (10) (1999) 797–804.
[105] J. Li, C. Fan, Q. Li, H. Wang, X. Zhang, In situ studies on irradiation resistance of nanoporous Au through temperature-jump tests, Acta Mater 143 (2018) 30–42.
[106] N. Nita, R. Schaeublin, M. Victoria, Impact of irradiation on the microstructure of nanocrystalline materials, J. Nucl. Mater. 329 (2004) 953–957.
[107] M. Loretto, P. Phillips, M. Mills, Stacking fault tetrahedra in metals, Scr Mater 94 (2015) 1–4.
[108] M. Kiritani, Story of stacking fault tetrahedra, Mater Chem Phys 50 (2) (1997) 133–138.
[109] D.S. Aidhy, C. Lu, K. Jin, H. Bei, Y. Zhang, L. Wang, W.J. Weber, Formation and growth of stacking fault tetrahedra in Ni via vacancy aggregation mechanism, Scr Mater 114 (2016) 137–141.
[110] L. Zhang, C. Lu, G. Michal, G. Deng, K. Tieu, The formation and destruction of stacking fault tetrahedron in fcc metals: a molecular dynamics study, Scr Mater 136 (2017) 78–82.
[111] T. Kadoyoshi, H. Kaburaki, F. Shimizu, H. Kimizuka, S. Jitsukawa, J. Li, Molecular dynamics study on the formation of stacking fault tetrahedra and unfaulting of Frank loops in fcc metals, Acta Mater 55 (9) (2007) 3073–3080.
[112] B. Wirth, V. Bulatov, T.D. de la Rubia, Atomistic simulation of stacking fault tetrahedra formation in Cu, J nucl mater. 283 (2000) 773–777.
[113] K. Nordlund, F. Gao, Formation of stacking-fault tetrahedra in collision cascades, Appl Phys Lett 74 (18) (1999) 2720–2722.
[114] J.W. Wang, S. Narayanan, J.Y. Huang, Z. Zhang, T. Zhu, S.X. Mao, Atomic-scale dynamic process of deformation-induced stacking fault tetrahedra in gold nanocrystals, Nat Commun 4 (2013) 2340.
[115] T.D. De La Rubia, R.S. Averback, R. Benedek, W. King, Role of thermal spikes in energetic displacement cascades, Phys. Rev. Lett. 59 (17) (1987) 1930.
[116] T.D. De La Rubia, M. Guinan, New mechanism of defect production in metals: a molecular-dynamics study of interstitial-dislocation-loop formation in high-energy displacement cascades, Phys. Rev. Lett. 66 (21) (1991) 2766.
[117] T. Daulton, M. Kirk, L. Rehn, In situ transmission electron microscopy study of ion-irradiated copper: comparison of the temperature dependence of cascade collapse in fcc-and bcc-metals, J nucl mater. 276 (1–3) (2000) 258–268.